

INTEGRATED AERODYNAMIC AND MECHANICAL DESIGN OF A LARGE-SCALE AXIAL TURBINE OPERATING WITH SUPERCRITICAL CARBON DIOXIDE MIXTURES

Abdelrahman Abdeldayem¹, Andrea Paggini³, Tommaso Diurno³, Claudio Orazi³, Martin White^{1,2}, Marco Ruggiero³, Abdulnaser Sayma¹

¹Thermo-Fluids Research Centre, School of Mathematics, Computer science and Engineering, City, University of London. EC1V 0HB, United Kingdom

²Thermo-Fluid Mechanics Research Centre, School of Engineering and Informatics, University of Sussex, Falmer, Brighton, BN1 9RH, United Kingdom

³Turbomachinery & Process Solutions, Baker Hughes, Via Felice Matteucci, Firenze, 50127, Italy

ABSTRACT

In this paper, the design of a large-scale axial turbine operating with supercritical carbon dioxide (sCO₂) blended with sulfur dioxide (SO₂) is presented considering aerodynamic and mechanical design aspects as well as the integration of the whole turbine assembly. The turbine is 130 MW, designed for a 100 MW_e concentrated-solar power plant with turbine inlet conditions of 239.1 bar and 700 °C, total-to-static pressure ratio of 2.94 and mass-flow rate of 822 kg/s. The aerodynamic flow path, obtained in a previous study, is first summarised before the aerodynamic performance is evaluated using both steady-state and unsteady 3D numerical models to simulate the aerodynamic performance of the turbine. Whole-annulus unsteady simulations are performed for the last turbine stage and the exhaust section to assess the unsteady loads on the rotor due to downstream pressure field distortion and to assess aerodynamic losses of the diffuser and exhaust section. The potential low engine order excitation on the last rotor stage natural frequency modes due to downstream pressure distortion is assessed. The design of the turbine assembly is constrained by current manufacturing capabilities and the proposed working fluid properties. High-level flow-path design parameters, such as pitch diameter and number of stages, are established considering a trade-off between weight and footprint, turbine efficiency and rotordynamics. Rotordynamic stability is assessed considering the high fluid density related to cross coupling effects. Finally, shaft end sizing, cooling system design and the integration of dry gas seals are discussed.

KEYWORDS

Axial turbine, sCO₂ mixtures, exhaust section, rotordynamic, thermal analysis, aeromechanical integration.

NOMENCLATURE

A	Sinusoidal amplitude of the vibration
C_{in}	Inlet absolute velocity [m/s]
C_{out}	Outlet absolute velocity [m/s]

C_{eff}	Effective damping coefficient [-]
C_{xx}	Damping force coefficient [-]
D_t	i^{th} stage bucket average pitch diameter [mm]
HP	The i^{th} stage maximum delivered power [W]
H_t	i^{th} stage bucket average height [mm]
J_{gen}	Rotor inertia [kg m ²]
J_{exp}	Rotor inertia of the expander [kg m ²]
$K.E$	Kinetic energy [kJ/kg]
K_{xy}, K_{yx}	Dynamic force coefficients [kN/mm]
\dot{m}	Mass flow rate [kg/s]
M_{ag}	Generator air gap malfunctioning torque [N.m]
$M_{se exp}$	Expander shaft end torque [N.m]
N	Rotational speed [RPM]
NPF	Nozzle passing frequency [Hz]
N_{R14}	Number of blades in the 14 th rotor
P	Static pressure [bar]
P_0	Total pressure [bar]
s	Specific entropy [J/kg.K]
t_1	time of first max oscillation [s]
t_{blade}	Time for one rotor blade pass [s]
T_d	Time period of the sinusoidal [s]
t_{rev}	Time for one complete rotor revolution [s]

Greek symbols

α	Exponential rate of decay of the oscillation
Δ	Difference
η_{tt}	Total-to-total efficiency [%]
σ	Max. equivalent stress [MPa]
ω	Pulsation frequency of the oscillation [Hz]

1 INTRODUCTION

Supercritical carbon dioxide power cycles (sCO₂) are promising candidates for concentrated solar power (CSP) plants [1, 2] where, the compression process takes place in the supercritical region using a compressor. The

SCARABEUS project [3], an EU funded project, is investigating the applicability and potential benefits of transcritical power cycles operating with CO₂-mixtures to produce 100 MW_e, where the working fluid is compressed in the liquid phase. This could result in enhanced power generation efficiency and bring the levelised cost of electricity (LCoE) of CSP plants to a competitive level compared to other dispatchable power generation plants operating in a renewable dominated energy market [4]. Several sCO₂ based mixtures have been proposed to increase the mixture's critical temperature, and hence allow for ambient air condensation in a transcritical power cycle for dry regions where water cooling is not available [3, 5]. The sCO₂-SO₂ mixture was found to be promising to increase the cycle thermal efficiency while offering a good thermal stability for the operating turbine inlet temperature [6]. Morosini, et al. [6] have shown that the adoption of sCO₂-SO₂ mixture instead of pure CO₂ increases the cycle thermal efficiency by 2% in the recompression configuration. Considering the environmental hazards, the optimum cycle performance, and the thermal stability of the candidate mixtures at 700°C, a molar mixture of 80% CO₂ and 20% SO₂ is used with a predicted overall cycle thermal efficiency of 51% [7].

Numerous studies have been dedicated to the aerodynamic design of axial turbines [8-10]. However, a complete design considering the whole turbine assessment integration is less commonly found. The aerodynamic flow path and the design of the mechanical components, such as blade modal analysis, thermal analysis, and rotordynamic stability are highly coupled [11-13]. A typical turbine design process comprises aeromechanical integration at different stages. The flow path design is initiated subject to mechanical design constraints such as stress limits and rotor slenderness ratio [14]. The optimised flow path design is then used to inform decisions related to different mechanical components such as cooling streams, casing design and shaft arrangement [12]. The geometrical limitations on the casing design, rotor stability, and cooling system affect the exhaust section which is aerodynamically optimised for performance subject to the given constraints. The exhaust section flow results are then used to quantify the alternating stresses on the blades as well as the pressure fluctuations at the interface between the last stage and the diffuser inlet [15]. These fluctuations are used in the modal analysis, while the alternating stress magnitude is used to assess the blade life and safety factor [16].

Several authors have presented the design of sCO₂ turbines of varying scales to reveal critical design considerations and the expected range of efficiencies. Zhang et al. [8] conducted a CFD analysis on a 15 MW single-stage axial turbine and predicted a total-to-static efficiency of 83.96%. Additionally, they demonstrated the significance of gas bending stresses on the turbine blades. However, the potential benefits of adding additional stages on the turbine performance were not investigated. On the other hand, Shi et al. [9] predicted a total-to-total efficiency of 92.12% may be achieved with a three-stage design for a 10 MW_e axial turbine. Moreover, they showed that the turbine can maintain 85% to 92% efficiency while operating at off-design conditions in the range of mass flow rates to the design mass flow rate from 62.5% to 110%. Total-to-total efficiency above 90% were also predicted by Bidkar et al. [10] for 4-stage and 6-stage 50 MW_e and 450 MW_e axial turbines, respectively. Kalra et al. [17] designed a four-stage axial

turbine for a 10 MW CSP plant. The study focused on practical considerations such as mechanical integrity, vibrational damping, sealing, shaft assembly, and operational transients. It highlighted the unique challenges imposed by sCO₂ turbines such as high torque transmission requirements, small aerofoil design and fabrication, aero-design optimisation with mechanically safe blade design, and high cycle fatigue life of the rotor. Wilkes, et al. [18] presented the design, manufacture, and testing of a 10 MW sCO₂ turbine for CSP application operating at 275 bar, and 700 °C inlet conditions. Thermal-structure interactions and fatigue analysis are presented for the expander casing. The results have shown that the project has successfully mitigated the risk of fatigue and creep while allowing for rapid thermal transients. Guédez, et al. [19] discussed the conceptual design of a 2 MW sCO₂ power cycle highlighting the proposed integration and operational regimes, expected thermodynamic performance at nominal point, and up-scaling considerations. These studies show the sCO₂ turbines performance and review previous iterations studying the turbine assembly integration. However, the performance of sCO₂ mixtures as well as the aero-mechanical components design integration are not presented.

The exhaust section in turbines is used to recover exit kinetic energy before the flow leaves the turbine. Numerous studies investigated the effect of the exhaust section on the performance of steam turbines [20-22]. Moreover, the exhaust section design generates low engine order frequency that needs to be considered for the blade modal analysis [22]. The accuracy of the overall diffuser performance prediction strongly depends on a proper coupling of both domains. The most accurate, but also most computationally expensive method is a transient full annulus simulation [20]. The design of the exhaust section has been extensively studied for large scale steam turbines. The common exhaust section design is of the radial type with an out box. This type of exhaust section can cause pressure non-uniformity at the interface between the exhaust section and the last rotor domain which has shown to cause a low frequency fluctuation in the aerodynamic force on the last stage rotor blades [15].

Numerous design challenges are introduced by the newly proposed working fluid selected for the SCARABEUS project [3]. The high gas density leads to high bending stresses meaning the blade chord length is increased, and the number of blades per stage is decreased [23]. The mean line design optimisation of the turbine has revealed that a large number of stages are required to reach high design point efficiency under the given operating conditions [7, 23]. Increasing the number of stages leads to a smaller hub diameter and longer blades introducing challenges related to the shaft lateral stability [24], and blade vibrations especially for the last rotor stage where the pressure fluctuations of the exhaust section dominate. The optimised cycle operating conditions for the selected working fluids also lead to technical challenges related to the cooling system, exhaust hood design, and material selection considering the manufacturability limitations.

In this paper, a comprehensive turbine design is presented for a 130 MW axial turbine operating with a sCO₂/SO₂ mixture of 80-20% molar composition. Both aerodynamic and mechanical design aspects as well as the integration of the entire turbine assembly are considered.

General mechanical design considerations are firstly discussed followed by a brief presentation of the flow path design and performance maps. The turbine exhaust section design is presented considering the integration with other mechanical design components. Detailed blade modal analysis, thermal analysis, rotor dynamic analysis, and torsional sizing analysis are presented for the proposed turbine design.

2 MECHANICAL DESIGN OVERVIEW

The high-level considerations driving the conceptual mechanical design of the turbine are summarised in this section. The power delivered by the turbine (≈ 130 MW) is such that the direct drive arrangement with a 2-pole synchronous generator is considered the only viable solution for this application. Although a geared design could be a feasible and convenient option for a smaller power rating (indicatively up to ≈ 50 -60 MW), it can be discarded a-priori for an application at such a high power rating based on practical experience.

Owing to the thermodynamic conditions at the inlet and outlet of the turbine, a barrel type external casing is selected with the aim to minimise radial deformations. The design has a horizontal split of the casing as shown in Figure 1 separating it into high pressure (HP) and low pressure (LP) sides with a vertical split flange connecting the two sides. The inlet flow is admitted into an inner casing, accommodating all the stator blade rows, having a split plane containing the rotational axis of the machine. Machining and assembly constraints introduced the necessity of splitting the exhaust section, which is designed in a separate casing, into two halves.

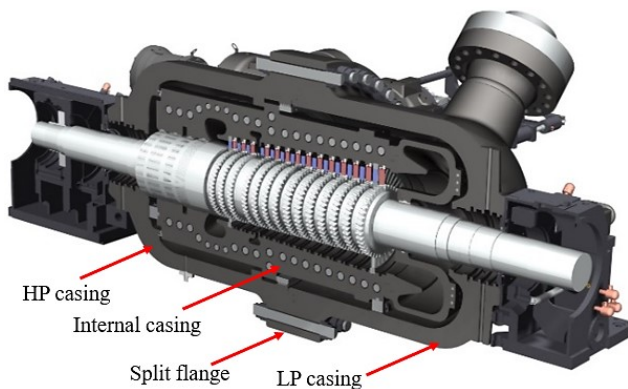


FIGURE 1: TURBINE ASSEMBLY CROSS SECTION © 2023 BAKER HUGHES COMPANY - ALL RIGHTS RESERVED

Material compatibility with pure $s\text{CO}_2$ at high temperature is presented in the literature [25]. However, no information is currently available about the compatibility with the working fluid used in this study. Industrial experience and supply chain considerations led to the decision to choose Ni-based alloys considering the high turbine inlet temperature and the poor characteristics of Martensitic steels, commonly used in ultra-supercritical (USC) steam turbines, with CO_2 . Studies have shown that 12% Cr Martensitic steels are prone to high temperature oxidation and carburisation when operated with CO_2 . Considering the current limitations applied to manufacturing of large castings and forgings in Ni-based alloys, it is decided to consider a limitation of approximately 20 tons for castings and 10 tons for forgings. Although these limits represent a

stretch of the current references of the Baker Hughes suppliers, it was deemed that it is possible to obtain a quality of the raw materials in line with the standard acceptance criteria employed for castings and forgings.

The tests carried out for the Desolation project have the goal to give high level indications about the compatibility of materials with the process fluid at high temperature [26]. The tests are aimed at identifying the alloys experiencing no or minimal interaction with the fluid as the promising materials in view of practical industrial applications. A testing campaign is ongoing to have a thorough material assessment through characterising the tensile and fatigue properties after a long exposure time.

The main design input that can be varied in the conceptual design phase is the rotor hub diameter as the rotational speed is fixed at 50 Hz. Whilst the aerodynamic design parameters, such as the loading coefficient, flow coefficient, degree of reaction and blade solidity can be optimised, the choice of the hub diameter has the most significant influence. For a small hub diameter, the flow path tends to have more stages, since the peripheral speeds of the stages are low, and the ratio between tip and hub radii is generally increased. Having a flow path with a small hub diameter is beneficial to limit the weight of the main components (rotor, inner casing and external casings), in line with the current manufacturing constraints. It is also beneficial for the torsional dimensioning of the rotor shaft ends as explained in Section 5.5.

Considering the hub diameter, dry gas seals (DGS) are selected to limit the leakage flows in view of a life cycle assessment (LCA) [27, 28]. Considering the limitations on the DGS technology, the shaft end diameter is in the order of 350-400 mm. The shaft end sizing is driven by the need to withstand the electrical malfunctioning torques such as short circuit and out-of-phase synchronisation, rather than the normal operating torque. More details are given in Section 5.5 about the torsional sizing. The smaller hub diameter results in high blade radius ratio, and hence interstage leakages have less impact on the turbine performance and the aspect ratio of the airfoils are more favourable. It is found that the hub diameter reduction encounters rotor-dynamic stability limitations as well; these aspects are discussed in Sections 5.4 and 5.2.

Cooling streams are designed for the turbine casings so that the necessity for using Ni-based alloys is removed to satisfy the current manufacturing limitations. Alternatively, 12% Cr stainless steel can be used for the external casings while Ni-based alloys are used for the rotor shaft, blades, inner casings, and trip & throttle valves. A cooling stream is designed at around 450°C as described in Section 5.3, to limit the oxidation and carburisation of 12% Cr Martensitic steel in a pure CO_2 environment [25]. However, it is yet to be ascertained whether this temperature is acceptable in case of working fluid containing SO_2 .

The Dry Gas seals are among the most critical components for the turbine mechanical design. The installation of these seals in $s\text{CO}_2$ turbines is challenged by the high pressure, high temperature, and high speed. These conditions lead to high thermal loads on the seal which significantly over complicates the design. The maximum allowable temperature by the DGS is limited to 220°C which

requires the employment of an additional cooling stream (at around 160°C) for the shaft end zones. In this regard, a dedicated thermal management system has been designed considering the findings proposed by the authors in another publication in which a segregated Conjugate Heat Transfer (CHT) numerical procedure has been presented and validated with experimental data provided by Flowserve with a rotating DGS test bench in sCO₂ environment [29, 30].

The material cooling requirements, along with the manufacturing capabilities, limits the design space for the aerodynamic optimisation of the exhaust section. Moreover, the geometry of the exhaust section is intrinsically prone to generating circumferential pressure non-uniformities downstream the last stage, which could pose concerns for the mechanical design of the last rotor stage. The exhaust section optimisation and the impact on the Goodman diagram of the last rotor stage are analysed in Sections 5.1 and 5.2.

3 NUMERICAL MODEL DESCRIPTION

Numerous 3D viscous CFD models are setup to simulate the aerodynamic performance of the proposed 14-stage turbine and the exhaust section. Firstly, a single passage steady-state CFD model of the 14 stages is setup to verify the mean line design results of the flow path and generate the turbine aerodynamic performance maps. Then, three different CFD models are setup that include the exhaust section to select the best geometry, study its effect on the entire turbine, and study its effect on the last stage, respectively. The first model is steady-state simulating the exhaust section in isolation to assess the aerodynamic performance of a given cross-section geometry. The second model is a steady-state single passage multi-stage CFD model simulating the interaction between the 14-stages and the exhaust section to quantify the effect of the exhaust section on the entire turbine performance. The third model is used to study the steady-state and unsteady circumferential variations caused by the exhaust section geometry on the last turbine stage, and is a full annulus simulation of all stator and rotor blade rows in the last stage along with the exhaust section as seen in Figure 2. The boundary conditions of the reference 14-stage model as well as the three models dealing with the exhaust section are summarised in Table 1.

TABLE 1: BOUNDARY AND OPERATING CONDITIONS OF THE DIFFERENT NUMERICAL MODELS

Parameter	Ref.	Model 1	Model 2	Model 3
Type	Steady	Steady	Steady	Steady + Unsteady
Geometry	14 St. (single)	Exhaust (E)	14 St. (single)+E	Last St. (Full)+E
Inlet total pressure [bar]	239	-	239	-
Inlet total Temperature [K]	973.15	829.0	973.15	839.2
Inlet mass flow rate [kg/s]	-	822	-	822
Outlet static pressure [bar]	81.24	81.24	81.24	81.24

The CFD models use shear stress transport (k- ω SST) turbulence model as it has been found to be the most suitable model for turbomachinery applications [31]. In the steady

state models, the interface between the stator and rotor domains is treated as a mixing plane which has been proven to give high quality results with the least numerical instabilities compared to the frozen rotor approach [32]. However, the interface between the last rotor blade and the exhaust inlet is frozen rotor to maintain the circumferential variations caused by the exhaust section geometry. All the interfaces in the unsteady model are sliding plane interface. The rotor is shrouded with a clearance gap between the shroud and the casing 0.07% of the tip diameter for each stage. The rotational speed is fixed at 3000 RPM.

The thermo-physical properties of the working fluid are evaluated using the Peng Robinson EoS [6, 33] and the properties are introduced through look-up tables generated to cover the expected pressure and temperature ranges with resolution of 500x500 points.

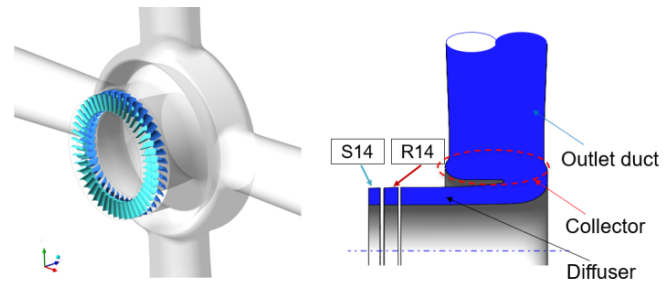


FIGURE 2: GEOMETRY DEFINITION OF MODEL 3: THE FULL ANNULUS OF THE LAST TURBINE STAGE WITH THE EXHAUST SECTION CROSS-SECTION

The unsteady simulation is setup in two models; the first model is initiated from the steady-state solution and advances over time for three complete rotor revolutions where $t_{rev} = 0.02s$ with a course time step of $t_{blade}/20$ to correct the initial steady-state solution and provide a more accurate transient performance for the detailed analysis. The blade passing time is calculated from $t_{blade} = t_{rev}/N_{R14}$ where N_{R14} is the 14th rotor number of blades = 42. This time step is selected based on iterative approach starting from 5 steps per blade pass while the obtained performance is found almost the same after 20 steps per blade pass. The second model is initiated from the last time step obtained from the first model and advances over time for 1 complete revolution with a finer time step of $t_{blade}/200$ to smoothly capture the blade load variations over time relative to a blade's position between the stator blades and the exhaust section outlet ports.

The meshing structure of the flow path is generated using TurboGrid solver built into ANSYS software version 2020R2. The sensitivity of the total-to-total efficiency to the average number of grid points per stage is reported in Figure 3 where it can be seen that 475k elements are required to get a tolerance relative to the finest mesh of 0.1%. The average number of grid points in the stator, and rotor blades is around 190k, and 285k elements, respectively. This difference is normally due to the tip clearance gap considered in the rotor domains.

The mesh of the entire geometry is controlled to get y^+ values between 30 and 100 where wall functions are best suited. The mesh structure of the exhaust section is completed using the ANSYS mesh solver where the elements size is

controlled considering a mesh independent entropy rise across the exhaust section and a symmetric pressure distribution on the exhaust section walls as reported in Figure 4. The mesh structure in the exhaust section is defined by 1.2 million grid points. The uncertainty of the exhaust section model calculated from the entropy rise values contributes to the entire turbine assembly by around 0.03%.

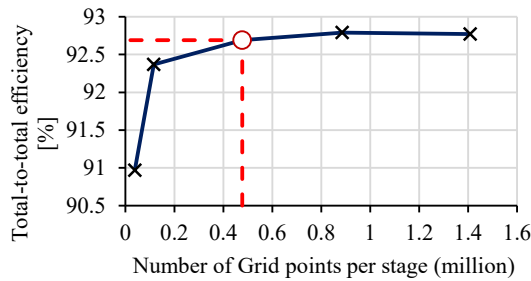


FIGURE 3 MESH SENSITIVITY ANALYSIS OF THE 14 STAGE REFERENCE MODEL

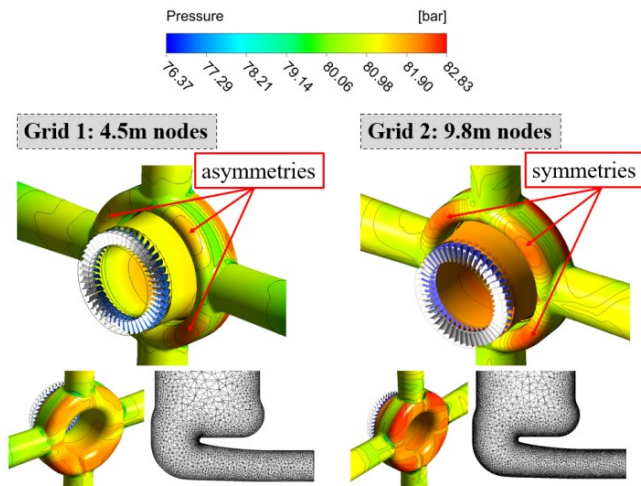


FIGURE 4: EFFECT OF GRID STRUCTURE ON THE PRESSURE DISTRIBUTION PATTERNS ON THE EXHAUST SECTION WALLS

Furthermore, a 3D finite element analysis (FEA) model is setup for the full rotor blades of the last stage to quantify the alternating stresses resulting from the exhaust section geometry. The aerodynamic loads (i.e., pressure distribution over the blade surfaces) predicted within the CFD simulations are transferred to the FEA model, along with the centrifugal load on the rotor blades due to rotation. The blades are fixed at the base of a 10 mm thick plate representing the hub surface with a fillet modelled between the blade and the base to introduce manufacturing allowance, and to avoid any numerically generated stress peaks at the sharp corner. For the FEA analysis, Nickel based alloys are potentially representing a good choice for the blades as they are commonly used with gas turbine blades that can operate at temperatures up to 1000 °C whilst maintaining a high yield strength suitable for the proposed operating conditions [34].

Both CFD and FEA model are verified against published numerical work for sCO₂ turbines in the authors' previous work [35].

4 TURBINE FLOW PATH DESIGN

The turbine blades are generated using the mean line results to create an initial geometry to initiate numerical analysis. Numerous design criteria are introduced to account for the proposed mechanical design limitations such as bending stress, and slenderness ratio [35, 36]. Design iterations made using mean line design model revealed that the total-to-total efficiency can be increased by increasing the number of stages and decreasing the hub diameter as reported in Table 2. Increasing the number of stages from 4 to 14 results in an increase in total-to-total efficiency of 6.9%, thus achieving a design total-to-total efficiency of 92.8% due to the reduction in peripheral speed from 194 to 107 m/s, and hub diameter reduction from 1.2 to 0.62 m. Increasing the number of stages beyond 14 stages marginally increases the total-to-total efficiency while the increase in slenderness ratio may have a negative effect on the rotor stability.

The off-design performance of the proposed models is investigated using the 3D numerical model and added to the comparison in Table 2. It is found that the 14-stage design has better turndown capability as it can run down to 41.8% of the design mass flow rate with an acceptable efficiency over 70% compared to 48.0% and 43.7% for the 4-stage and 9-stage designs, respectively. The efficiency gain by selecting the 14-stage design at half load is calculated 8.31%, and 2.57% compared to the 4-stage, and 9-stage models, respectively.

TABLE 2 COMPARISON BETWEEN DIFFERENT NUMBER OF STAGES

Parameter	4-stage model	9-stage model	14-stage model
Hub diameter [m]	1.21	0.81	0.62
Flow path length [m]	0.52	1.0	1.8
Inlet Mach number [-]	0.46	0.31	0.25
Total-to-total efficiency at the design point [%]	85.86	92.11	92.81
Total-to-total efficiency at 50% mass flow rate [%]	72.38	78.12	80.69
Minimum mass flow ratio to the design point [-], $\eta_{tt} > 70\%$	0.480	0.437	0.418

A 3D numerical CFD model is setup to verify the mean line design and initialise the 3D blade shape optimisation. The blades geometry is initiated using the 1D mean line design parameters in addition to some geometrical assumptions which are optimised in a subsequent design stage to give the best possible performance. Cylindrical turbine blades are assumed due to the small blade height to mean diameter ratio of 0.07 on average. The key design parameters are reported in Table 2, where it can be seen that the CFD predicts a 92.8% total-to-total efficiency and a total power production of 132 MW power, as required for a 100 MW_e power cycle for a CSP plant [3]. It worth mentioning here that total-to-total efficiency is obtained for the flow path excluding any leakage flow streams except for the rotor tip leakage.

The turbine performance is further improved by blade shape optimisation as explained in the author's previous work [35], where the constraints limit the maximum allowable equivalent stress and the mass flow rate within 2% of the cycle design mass flow rate. The volute optimisation challenges are mainly linked to the number of decision variables

that can fully represent the profile shape. In addition, the high working fluid viscosity and density have increased the blade loading and the mass flow rate sensitivity to the blade profile geometry. In this case, the optimisation objective is more restricted to satisfy the system constraints rather than achieving the best aerodynamic performance.

A comparison between the reference and optimised blades has shown an increase in the total-to-total efficiency from 90.2% obtained from the initial blade model to 92.8% for the optimised geometry. The optimised geometry for the first stage shows only slight variations when compared to the last stage. This is because turbulence is much lower at the turbine inlet compared to the cumulative turbulence effects at the final stages. As a result, the inlet wedge angle is significantly increased in the last stage from 15° to 26° to account for the larger flow angle deviation from the blade angle and limit the flow separation.

5 RESULTS AND DISCUSSION

After the flow path design phase is completed and the 3D blades are finalised, the complementary design aspects are initiated. These include the exhaust section design, the blades modal analysis, thermal analysis, rotordynamic analysis, and shaft torsional sizing.

5.1 Exhaust section aerodynamic performance

Exhaust sections are normally used in axial turbines to recover part of the kinetic energy into pressure with the least possible aerodynamic losses. Due to space limitations driven by the design of the cooling system and by rotor-dynamic constraints, a new exhaust section is proposed instead of the commonly used radial exhaust with outlet box, that is typically used in large scale steam turbines, as illustrated in Figure 1 of the proposed exhaust section integrated within the turbine assembly, and Figure 2 of the numerical domain. The reference diffuser and collector cross-section geometry has been designed between 580:1310 mm radial location, and 1680:2250 mm axial location with an area ratio of 1.17 for the diffuser part. Different geometry cross sections and the number of outlet ducts have been iterated to achieve the best aerodynamic performance whilst considering to mechanical constraints. The reference cross section is designed as an initial guess aiming at utilising the available space and make the diffuser section as long as possible. Numerous modifications are tried while the selected cross sections are M_1 , M_2 , and M_3 . M_1 is designed to increase the diffuser area ratio while keeping the sharp turn between the diffuser and collector. M_2 is modified by decreasing the diffuser length to facilitate the flow turn between the diffuser and collector while the diffuser section is almost removed in the M_3 section to further improve the flow turn. The modified diffuser and collector cross-sections relative to the reference cross-section are summarised in Figure 5.

A set of numerical models are setup for the different cross sections as defined in Table 1 with two and four outlet ducts. The expansion enthalpy-entropy diagram is plotted for the different models as reported in Figure 6 where E_2 , and E_4 correspond to two and four outlet ducts, respectively, and the R , M_1 , M_2 , and M_3 are the reference, modification 1, modification 2, and modification 3 cross sections, respectively. In the figure, each curve is represented by 3 points where the first and second points are for the diffuser

inlet and outlet while the end point is the outlet from the exhaust ducts. As can be seen from the figure, the two outlet designs (E_2) record higher total entropy rise due to the long circumferential distance between the outlet ports which increases the distance a flow needs to cover until reaching the outlet. For the E_2 models, the outlet kinetic energy is still high because of the limited outlet cross-sectional area. By comparing the different cross sections, it can be seen that the M_2 design has the lowest entropy rise and hence the best aerodynamic performance with both E_2 and E_4 options.

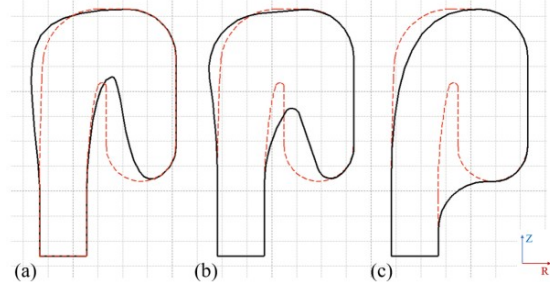


FIGURE 5: MODIFIED DIFFUSER AND COLLECTOR CROSS-SECTIONS RELATIVE TO THE REFERENCE CROSS-SECTION. (A) M_1 , (B) M_2 , AND (C) M_3

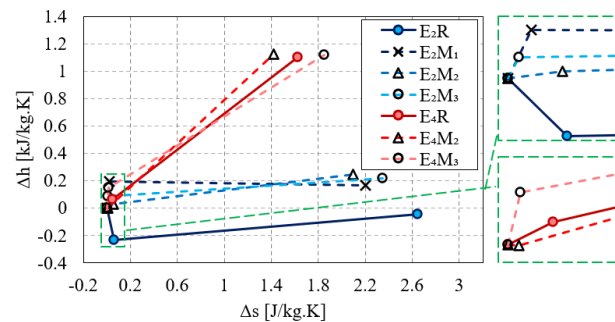


FIGURE 6: ENTHALPY-ENTROPY DIAGRAM OF THE DIFFERENT EXHAUST GEOMETRIES. DIFFERENT CROSS SECTIONS AND DIFFERENT NUMBER OF OUTLET DUCTS. LEFT: FULL DATA, AND RIGHT: ZOOM IN

Furthermore, the breakdown of the entropy rise is investigated as shown in Figure 7. It is noted that the losses in the diffuser section are almost negligible while the collector and outlet ducts dominate the performance. The E_4M_2 design corresponds to the lowest total losses with the lowest amount of entropy rise in the outlet ports. By comparing the E_2 and E_4 designs, it can be seen that the collector losses are higher in the E_2 design as discussed. By comparing the M_3 and the M_2 cross-sections, the M_3 geometry has minimum flow restrictions in the collector domain, designed to give better aerodynamic performance, however, this design has records higher total losses. Although the M_3 design has achieved lower collector losses, the losses in the outlet ducts are the highest as the flow towards the ducts is unguided and generates more turbulence. The total entropy rise, loss in total pressure, and change of kinetic energy across the exhaust section are summarised and compared in Table 3 where the results agree with the observations made from Figure 6 and Figure 7. It can be noted from the table that increasing the number of outlet ducts from 2 to 4 using the M_2 cross-section decreases the entropy rise across the exhaust section by 32%. By comparing the entropy rise across the exhaust section to the entropy rise across the 14-stages which is calculated around 14.8 J/kg.K, it can be calculated

that increasing the number of outlet ducts to 4 decreases the whole turbine losses by around 4%.

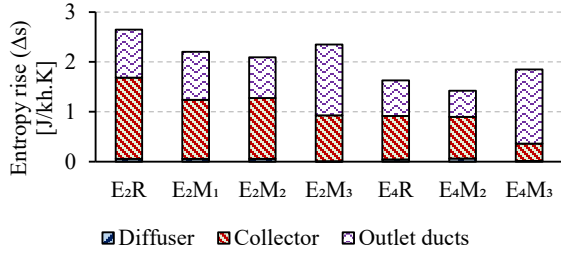


FIGURE 7: LOSS BREAKDOWN ANALYSIS OF THE EXHAUST HOOD FOR THE DIFFERENT GEOMETRIES

TABLE 3: COMPARISON BETWEEN THE DIFFERENT CROSS SECTIONS AND DIFFERENT NUMBER OF OUTLET DUCTS OF THE EXHAUST SECTION

Model	E_2R	E_2M_1	E_2M_2	E_2M_3	E_4R	E_4M_2	E_4M_3
ΔS_{total} [J/kg.K]	2.65	2.20	2.10	2.35	1.63	1.42	1.85
$\Delta P0_{total}$ [bar]	-1.25	-1.05	-0.98	-1.11	-0.76	-0.66	-0.85
C_{out} [m/s]	52.8	48.9	47.9	47.9	24.9	24.4	25.0
C_{in} [m/s]	52.4	52.6	52.7	52.6	53.1	53.2	53.1
$\Delta K.E$ [kJ/kg]	0.02	-0.19	-0.24	-0.24	-1.10	-1.12	-1.10

The flow field in the different cross sections is further explored and reported in Figure 8 for the reference cross-section and Figure 9 for the three proposed modifications. The diffuser section of the reference design (E_2R) is found to accelerate the flow instead of diffusing it due to the flow pattern which creates an effective flow area ratio less than 1 as shown in Figure 8. The large counter-rotating vortex at the end of the collector section of the reference design increases the losses. The size of this vortex is decreased significantly in the first two modifications (M_1 , M_2) and completely avoided in the third modification (M_3). By investigating the collector section, it has been found that the M_3 design shows the lowest collector losses; however, this design didn't give the best overall exhaust section performance. The best combination between collector and outlet ducts losses is found with the M_2 cross-section with 4 outlet ducts. Thus, this geometry is selected for the final turbine design.

The aerodynamic interaction between the turbine stages and the exhaust section is studied by solving single passage 14-stage CFD model with exhaust section for the reference and M_2 models. The change in the power produced per stage is calculated for the two models with respect to the reference 14-stage model without exhaust section and the results are plotted in Figure 10. Although the exhaust sections in turbines are designed to recover pressure and increase the power output, the power produced from the proposed turbine is slightly reduced because of the special geometrical limitations on the proposed exhaust section which increase the aerodynamic losses. In the meanwhile, the design kinetic energy at the last stage outlet is not sufficiently high to cover the developed aerodynamic losses and generate positive pressure recovery. As seen in the figure, the last stage is the most affected by the exhaust section with a drop of around 2% of the reference value for the M_2 model. This effect is

found to decrease for upstream stages with a change in power production of less than 0.1% for the first stage in the M_2 model. By comparing the reference and modified cross section geometries of the exhaust sections, it appears the reference geometry causes a larger power drop due to higher aerodynamic losses as explained in Table 3.

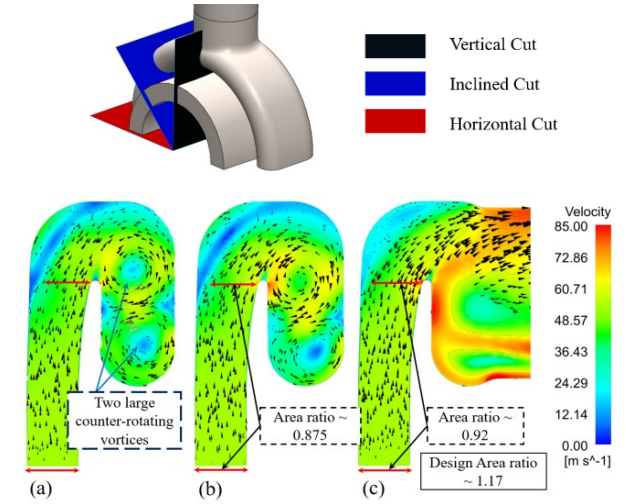


FIGURE 8: FLOW FIELD IN THE REFERENCE DIFFUSER AND COLLECTOR CROSS SECTION AT: (A) HORIZONTAL CUT, (B) INCLINED CUT, AND (C) VERTICAL CUT

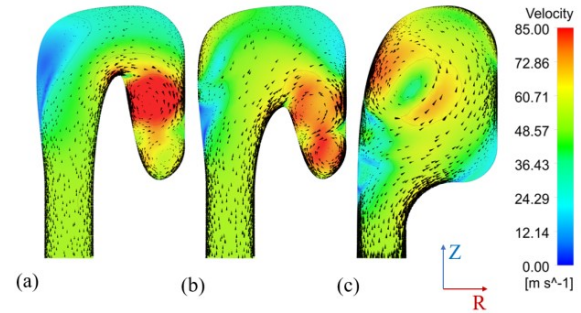


FIGURE 9: FLOW FIELD IN THE DIFFERENT CROSS SECTION MODIFICATIONS AT AN INCLINED CUT MIDWAY BETWEEN THE PERIODIC PLANE AND THE OUTLET DUCT. (A) M_1 , (B) M_2 , AND (C) M_3

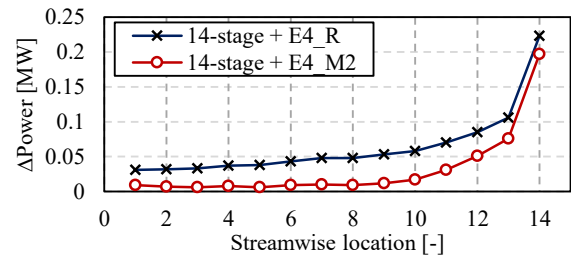


FIGURE 10: THE DROP IN POWER PRODUCED PER STAGE WITH RESPECT TO THE REFERENCE 14-STAGE MODEL WITHOUT EXHAUST SECTION

The results of the 14-stage model with and without the exhaust section are summarised in Table 4 which has showed a slight increase in the total-to-total efficiency obtained using the E_4M_2 exhaust section due to the achieved pressure recovery. The power produced by the whole turbine as well as the mass flow rate with and without the exhaust section are almost the same.

TABLE 4: COMPARING THE PERFORMANCE OF THE 14-STAGES WITH AND WITHOUT THE EXHAUST SECTION FOR THE R AND M2 CROSS-SECTIONS

Model	14-stage	14-stage + E_4R	14-stage + E_4M_2
\dot{m} [kg/s]	822.892	822.062	822.646
Power [MW]	130.103	129.198	129.655
η_{tt} [%]	92.89	92.82	92.98

Although the effect of the exhaust section on the aerodynamic performance of the whole turbine is not significant, the potential forced excitation, that might be detrimental for the rotor blade dynamic behavior, needs to be investigated. These excitations are expected due to the number of outlet ducts which affects the pressure distribution downstream of the last rotor stage. Full annulus of the last stator and rotor blades are modelled with the exhaust section as explained in Figure 2 while steady and unsteady performance is evaluated.

A comparison between steady-state and the time averaged unsteady performance of the last stage (SR) and the exhaust section (E) are reported in Table 5. The comparison between the steady M_2 and R models confirm the previous observations where the loss in total pressure and entropy rise across the exhaust section are higher in the reference model. By comparing the steady and unsteady performance of the M_2 model, it can be seen that the unsteady losses are slightly higher as the entropy rise across the stage and the exhaust domain are both higher. However, the drop in total pressure is around 0.8% lower in the unsteady model and the power produced is less by 1.6%.

The unsteady variation of the total-to-total efficiency of the last turbine stage full annulus model is shown in Figure 11. The time shown in the figure corresponds to 10 complete rotor revolutions as the revolution time is 0.02 s. A convergence has been achieved after around 5 complete revolutions while the difference between the steady-state and unsteady state solution is found within 0.4%. After 5 revolutions, the total-to-total efficiency value keeps oscillating within 0.02% which defines the unsteady model uncertainty.

TABLE 5: COMPARING THE PERFORMANCE OF THE REFERENCE AND MODIFIED EXHAUST SECTIONS IN THE FULL ANNULUS MODEL. (SR) STANDS FOR THE LAST TURBINE STAGE, AND (E) STANDS FOR THE EXHAUST SECTION

Model	$SRE E_4R$ (Steady)		$SRE E_4M_2$ (Steady)		$SRE E_4M_2$ (Unsteady)	
	SR	E	SR	E	SR	E
ΔP_0 [bar]	7.56	1.57	7.56	1.27	7.50	1.27
Δs [J/kg.K]	0.79	3.44	0.79	2.74	0.89	2.78
ΔP [bar]	7.62	0.86	7.66	0.53	7.53	0.59
C_{exit} [m/s]	55.80	24.70	56.06	24.74	55.78	24.09
Power [MW]	9.86	-	9.95	-	9.79	-

The steady state fluctuation of aerodynamic force magnitudes on a rotor blade of the last stage is presented in Figure 12 along with the corresponding maximum equivalent stresses obtained using FEA analysis of the blade. In the figure, the normalised rotor circumferential position is the blade angular position divided by 360°. It can be seen that the steady state model does not clearly predict the peaks

corresponding to the number of outlet ducts as the force magnitudes are not only dependent on the rotor blade position relative to the outlet ports but also the relative position corresponding to the upstream stator blades which cannot be predicted using the stage mixing plane interface.

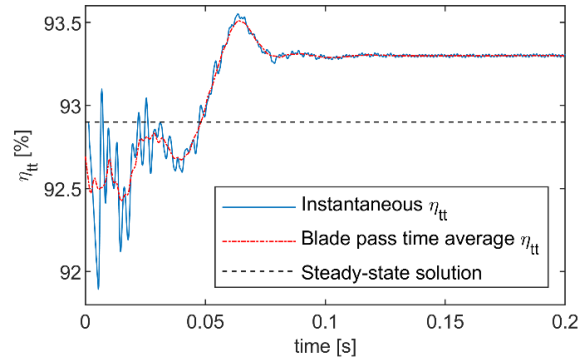


FIGURE 11 UNSTEADY VARIATION OF THE TOTAL-TO-TOTAL EFFICIENCY OF THE LAST TURBINE STAGE

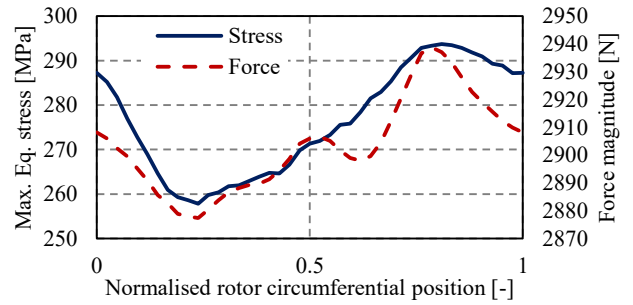


FIGURE 12: AERODYNAMIC FORCE MAGNITUDES ON THE LAST ROTOR BLADES ALONG THE CIRCUMFERENTIAL DIRECTION OBTAINED FROM THE STEADY STATE MODEL

A more accurate prediction can be obtained using the sliding plane interface between the stator/rotor and the rotor/exhaust in the unsteady model. The unsteady model is initiated using the steady state solution and advanced in time for three complete revolutions until the fluctuation in inlet total pressure and the entropy rise across the exhaust section are periodic. The results of the unsteady force fluctuation on the last stage rotor blades are given by Figure 13 for one complete revolution starting after the three revolutions of the first model. The results show variations between 3050 N to 3143 N compared to 2877 N to 2939 N obtained using the steady-state model with around 6.1% difference of the mean value. The variation in the maximum equivalent stresses is evaluated using both models and applied to the Goodman diagram reported in the following section.

The force fluctuation in the time domain is converted into the frequency domain, as reported in Figure 14, to evaluate and compare the strength of the dominant frequencies. A strong effect of the frequency corresponding to 4 times the rotational frequency (4xREV) is observed compared to the main frequencies, 42xREV and 47xREV corresponding to the number of rotor and stator blades, respectively. The 4xREV frequency corresponds to the number of outlet ducts downstream of the last stage rotor, however, frequencies corresponding to the number of stator and rotor blades of that stage are stronger. The figure has shown that the frequency corresponding to the number of outlet ports decreases significantly starting from the 8xREV

frequency which is cut to 74% compared to the 4xREV frequency. More details about the blade mechanical analysis are given in section 5.2.

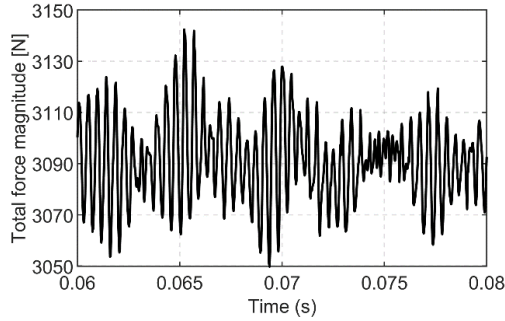


FIGURE 13: TOTAL FORCE MAGNITUDE FLUCTUATION ON THE LAST ROTOR BLADES OVER TIME FOR ONE COMPLETE ROTOR REVOLUTION

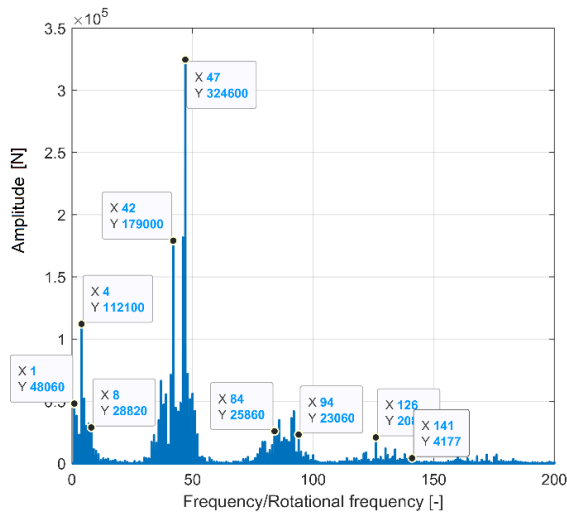


FIGURE 14: FREQUENCY DOMAIN OF THE BLADE FORCE WAVE GIVEN IN FIGURE 13

5.2 Blade mechanical analysis

The design chosen for the rotating blades is with firtree root and integral shroud. The firtree geometry allows a radial dimension of the root that is much smaller compared to a simpler T-root design, which would have been feasible due to the low peripheral speed of the final flow path selected (106 m/s for the 1st stage and 116 m/s for the last one); this choice results in a larger stiffness diameter of the rotor in the flow path region which is beneficial for the rotor-dynamic stability.

The chords of the airfoils, selected preliminarily targeting static stresses acceptable for the creep limit of the material, have been found to also produce an acceptable design from a dynamic point of view. The natural frequencies are sufficiently spaced away from the potential excitations as can be seen in the SAFE diagrams of the first and last rotor stages (Figure 15 and Figure 16). Moreover, despite the absence of critical resonances, it has been confirmed that, for last rotor stage, the alternate stresses generated by the non-uniform circumferential distribution of the pressure downstream are acceptable in terms of high cycle fatigue; Figure 18 reports the Goodman diagram of the stage in dimensionless form.

Nickel-based alloys represent a good choice for the blades in reason of the good mechanical properties (primarily creep and HCF). As already remarked, the compatibility with the process fluid is yet to be ascertained. The geometrical characteristics of 1st and 14th stages are reported in Table 6.

Although the application is at fixed speed (3000 rpm), the SAFE diagram reports the harmonics of 95% speed and 105% speed to ensure that no critical encroachments are present in the vicinity of the synchronous speed. The potential sources of excitation considered are the nozzle passing frequency (1xNPF), 2xNPF, low harmonics of the rotating speed (up to 15xREV), (number of upstream blades – number of blades), and (number of downstream blades – number of blades).

TABLE 6: THE GEOMETRICAL CHARACTERISTICS OF 1ST AND 14TH STAGES

Stage	1 st stage	14 th stage
Hub diameter [mm]	620	620
Blade height [mm]	28.7	59.2
No. of vanes upstream	58	47
No. of buckets	53	42
No. of vanes downstream	57	-
Young's modulus [MPa]	164	174

Concerning the 1st stage (Figure 15) it is observed that no encroachments are present neither with NPF nor with 2xNPF. The potential excitations (number of upstream blades – number of blades), and (number of downstream blades – number of blades) are not critical, since they do not encroach any natural mode of the stage. The first encroachment with the harmonics of the rotating speed (with the additional margin +/- 5%) is with the 47th mode, which is a very high harmonic order, and not critical for the mechanical design of the stage.

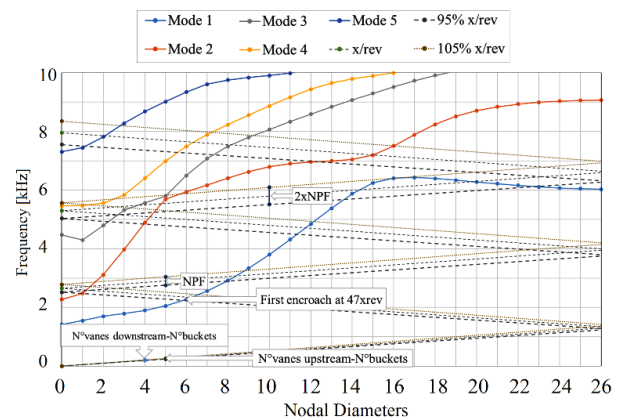


FIGURE 15: SAFE DIAGRAM OF THE 1ST ROTOR STAGE © 2023 BAKER HUGHES COMPANY - ALL RIGHTS RESERVED

Concerning the 14th stage (Figure 16) it is observed that the NPF is not encroaching any natural modes of the stage whereas 2xNPF has a 5% margin with respect to the 3rd mode which, nonetheless, is the minimum separation margin acceptable. The potential excitation (number of upstream blades – number of blades) is not critical, since it does not encroach any natural mode of the stage. The first encroachment with the harmonics of the rotating speed (with the additional

margin +/- 5%) is with the 35th mode, which is a very high harmonic order, and not critical for the mechanical design of the stage.

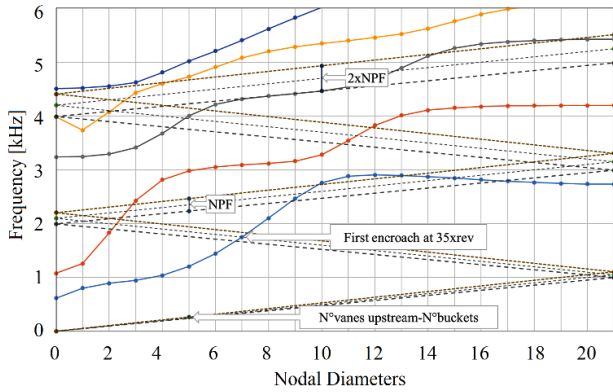


FIGURE 16: SAFE DIAGRAM OF THE 14TH ROTOR STAGE © 2023 BAKER HUGHES COMPANY - ALL RIGHTS RESERVED

The fluctuations of the maximum equivalent stresses on the last stage rotor blades, obtained using both steady and unsteady CFD calculations, are used to plot the Goodman diagram. The Goodman diagram of the last rotor stage is shown in Figure 18, where it can be seen that the alternate excitations are largely within the high cycle fatigue (HCF) capability of the blade material.

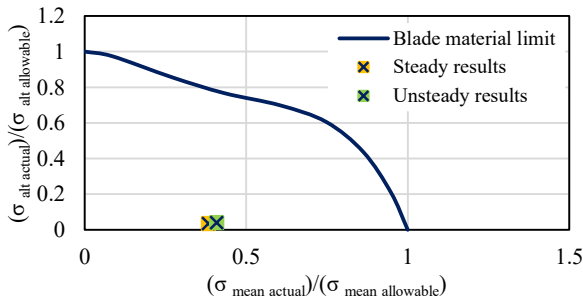


FIGURE 18: DIMENSIONLESS GOODMAN DIAGRAM FOR THE LAST ROTOR STAGE © 2023 BAKER HUGHES COMPANY - ALL RIGHTS RESERVED

5.3 Thermal analysis

Due to the high inlet temperature of 700 °C, an external cooling flow is utilised to cool both the rotor balancing piston and the external casing. In this case, 12Cr steel material can be used for the external casing, avoiding the need for superalloys. A schematic representation of the cooling flows is reported in Figure 17 together with the thermal field obtained with a 2D axisymmetric model of the expander. This cooling system has been designed with the commercial fluid network solver “Altair Flow Simulator”, which iteratively solves conservation of mass, momentum, angular momentum and energy, giving a punctual set of results in term of pressure, temperature, swirl, and mass flow rate.

The cooling flow (2.2% of the expander exhaust flow) is injected into the internal casing (main cooling flow) and is over pressurised compared to the expander inlet pressure. The cooling flow is split into two streams; a small stream flows to the right through seal N°1 which is reintegrated into the main flow path while the larger cooling flow stream is directed towards the balancing chamber through seal N° 2. The mass flow distribution is controlled by the number of teeth of the seals resulting from a sensitivity analysis aiming primarily at minimising the total cooling flow for a fixed pressure drop to limit the impact on the cycle thermal efficiency. The teeth distribution of seals N° 2, 3, and 4 are optimised to provide the proper cooling flow for the casing chambers.

The High-Pressure Chamber (HPC) cooling flow is reintegrated into the flow path at the third stage after cooling the HP chamber between internal and external casing. The Low-Pressure Chamber (LPC) cooling flow is split into two streams after feeding the LP casing chambers; the larger stream is reintegrated into the exhaust hood via properly dimensioned orifices while the remaining mass flow rate is directed towards the rear DGS. This stream is reinjected in the flow path via seal N° 5 after mixing with Rear DGS cooling flow. Finally, the remaining cooling flow in the balancing chamber flows through seal N°4 in the balancing chamber where it mixes with the front DGS cooling flow and reintegrates into the exhaust hood.

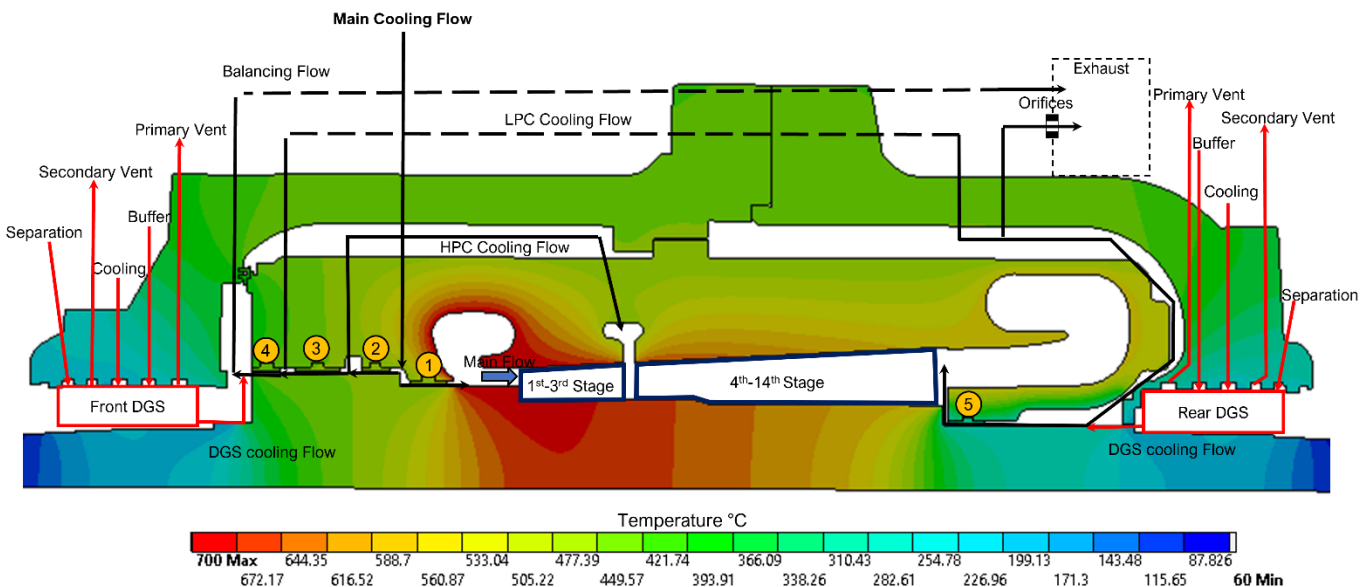


FIGURE 17 SECONDARY FLOW SCHEME AND THERMAL MAP © 2023 BAKER HUGHES COMPANY - ALL RIGHTS RESERVED

Once the fluid network is designed, the Heat Transfer Coefficients (HTC) are computed using appropriate correlations and imposed, together with fluid bulk temperature, as boundary conditions for the thermal model. The temperature map of the expander is reported in Figure 17. The effect of the balancing piston cooling flow is clear with a strong axial gradient between this region and the expander inlet. This cooling primarily aims at cooling the HP and LP casing chambers, which are around 450 °C, while as a positive side effect it decreases the temperature of the rotor shielding the shaft-end region by the hot inlet temperature, and consequently reducing the cooling flow required by the front DGS. Indeed, the maximum allowable temperature of DGS of around 220° C requires the design of a dedicated thermal management system, which consumes less than 0.5 % of the total expander mass flow (considering the two DGSs) to counter both the significant internal viscous heat and the external heat transferred by conduction from the hot region of the expander.

The DGS cooling system has been designed in light of the findings proposed by the authors in another publication, in which a segregated Conjugate Heat Transfer (CHT) numerical procedure, suitable for DGS thermal design, has been presented and validated with experimental data provided by Flowserve with a rotating DGS test bench in sCO₂ environment [30]. The cooling system uses process gas at 160 °C to maintain the front seal at temperatures around 200 °C, while the rear one presents a slightly higher temperature due to the current secondary flow scheme. Indeed, the LP cooling flow, which is sCO₂ at 450 °C, warms up the rear external casing above the DGS, which is averagely hotter with respect to the front one. This heat is transferred to the seal via conduction, and consequently a higher cooling mass flow rate is required with respect to the front DGS to limit the temperature at 220 °C.

Most of the cooling flow streams are reinjected into the machine after cooling the DGS, while a negligible part flows into the primary vent together with the buffer gas (pure CO₂). This mixture is recompressed and reintegrated back to the cycle. It is worth mentioning how the mixing between process and buffer gas alters the process gas composition, which shall be monitored and controlled during the expander operations. The secondary vent is fed, instead, with a mixture between buffer (CO₂) and separation gas (air).

5.4 Rotordynamic analysis

Lateral rotordynamic behaviour for a flexible rotor and high energy density can be heavily affected by the stability of the vibration modes, especially the first forward mode in a “between bearings” rotor configuration. The practical way to estimate the margin for rotor instability is the logarithmic decrement (LogDec) of the non-synchronous as given by equation [1].

$$\text{LogDec} = \ln \left(\frac{Ae^{-\alpha\omega t_1}}{Ae^{-\alpha\omega(t_1+T_d)}} \right) = \alpha\omega T_d \quad (1)$$

The main factor that can affect the rotor stability are the Alford effect and the seals effect. The Alford effect is related with the additional torque introduced by the non-circumferential uniform pressure distribution along the expander stages. The seals’ effect is related to the interaction

between the fluid and rotor-stator surface that leads to additional energy to precession whirling (typically the forward one) able to increase the lateral amplitude vibration. All those effects can be summarised on the LogDec stima; in case it is negative, the relevant mode vibration amplitude shall increase until non linearities effect raise up.

Dealing with a novel turbine design adds additional design challenges related to mechanical stability. The sub-synchronous vibration, at the relevant frequency mode, is considered the most important contributor to the overall vibration. Once an instability effect is triggered, it cannot be controlled because the effects are related to the dynamic system itself (i.e., position of pole into the root locus). Usually, major modifications have to be considered to avoid high frequency instability such as; changing clearances, rotor shape, designing additional dampers, modifying the geometry and type of seals, adding swirl breakers, and changing the type of bearings.

The starting point of the analysis is the rotor + bearing stability check including the effect of the rotor-bearing interaction. The dynamic model configuration developed includes the rotor hot material properties, and minimum bearing clearances (Figure 19). From this point the effects are added in the model as a constraint between rotor and stator. Those constraints are identified as dynamic force coefficient.

The Alford effect dynamic force coefficient are estimated as API 612 8th edition using equation [2].

$$K_{xy} = -K_{yx} = \sum_{i=1}^n \left(\frac{HP \cdot B_t \cdot C}{D_t \cdot H_t \cdot N} \right)_i \quad (2)$$

where, $B_t = 1.5$, and $C = 9.55$

Seal dynamic effects are estimated using an internal modelling tool called “SEALAB” that considers several geometrical details in terms of seals, rotor configuration, and thermodynamic fluid properties. Once the fluid dynamic steady-state equation (0th order) is solved (i.e., the steady state distribution of pressure, fluid swirl ratio, and flow across the seals) a perturbation is applied in the equilibrium state. The linearised relationship between the rotor motion and the force are calculated as reported in Figure 20 where the dynamic force coefficient is calculated.

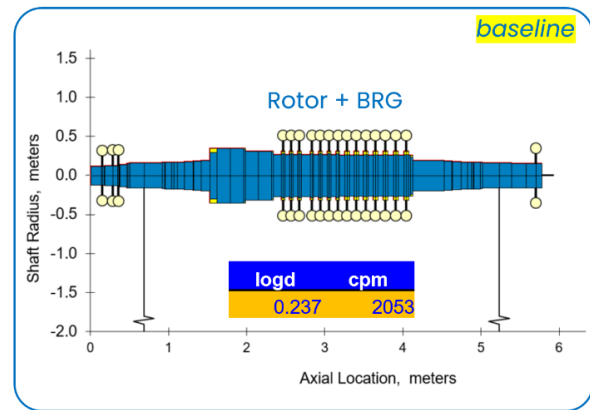


FIGURE 19 ROTOR + BRG ROTORDYNAMIC MODEL © 2023 BAKER HUGHES COMPANY - ALL RIGHTS RESERVED

Seals that are included in the SCARABEUS model are: inner casing seal, and balancing drum seals (inner and outer).

The dynamic effect of the seals can be easily summarised by measuring the effective damping force coefficient as shown in equation [3].

$$C_{eff} = C_{xx} - \frac{K_{xy}}{\omega} \quad (3)$$

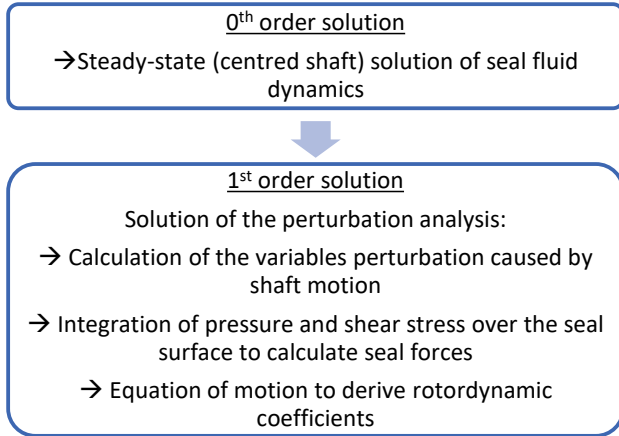


FIGURE 20 SEALAB BULK-FLOW MODELLING PROCEDURE © 2023 BAKER HUGHES COMPANY - ALL RIGHTS RESERVED

It is well known from the literature that the tangential force can act as stabilising or de-stabilising factor [13, 37]. Damping acts as stabilising force that tends to reduce the rotor precession whirling, the opposite is the cross-coupling stiffness contribution as shown in Figure 21.

For a novel turbine design, the force dynamic coefficient estimation and the overall stability analysis can significantly affect the mechanical layout and rotor-dynamic verification. The dynamic behaviour predictability is challenging for a rotor prone to mode instability, such as flexible rotors used for high density applications with high operational speed.

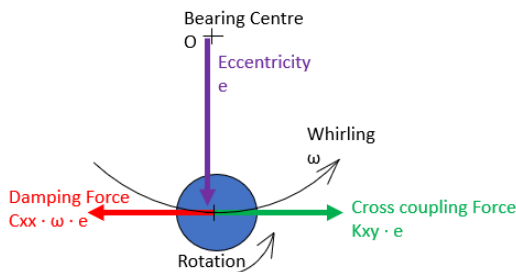


FIGURE 21 EFFECTIVE DAMPING FORCE SCHEMA © 2023 BAKER HUGHES COMPANY - ALL RIGHTS RESERVED

The effect of seals is dependent on some parameters such as; clearances, fluid thermodynamic properties across the seal, geometry (full labyrinth, half labyrinth, abradable), and pre-swirl (PS) defined as the tangential fluid velocity component over the local rotor speed at the input side of the seal. Lower pre-swirl leads to a lower destabilising effect acting on the rotor. High value of the pre-swirl on the seal turns the C_{eff} highly negative producing a destabilising effect on the first forward mode. In this case a swirl brake device able to reduce initial pre-swirl on the seals can lead to a positive effect. Considering all the described destabilizing effects, the dynamic behaviour of the rotor results a stable condition as seen in Figure 22.

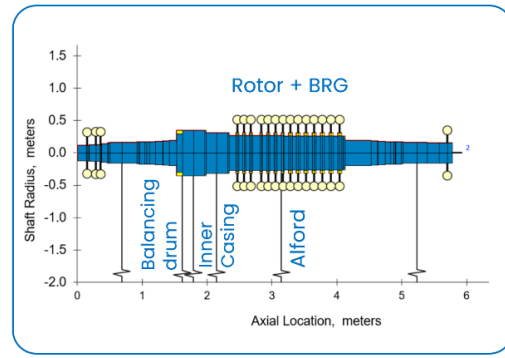


FIGURE 22 ROTOR + BRG IN ADDITION TO ALL DESTABILIZING EFFECTS INCLUDED IN THE MODEL © 2023 BAKER HUGHES COMPANY - ALL RIGHTS RESERVED

5.5 Torsional sizing

A preliminary torsional sizing can be done with rigid torsional considerations for the proposed expander rated for 130 MW, assuming a power factor of 0.85 that results in a synchronous generator sized for 153 MVA.

Based on data of electrical generators of a similar power rating, the rotor inertia (J_{gen}) of a 153 MVA, 2-poles, electrical generator is estimated around 4000 kg m². The rotor inertia of the expander (J_{exp}), for the proposed 14-stage, 620 mm hub diameter design is 320 kg m². An electrical malfunctioning torque (short circuit or out-of-phase synchronization) occurring at the generator air gap (M_{ag}), discarding possible amplifications generated by torsional resonances, results in a torque at the expander shaft end ($M_{se exp}$) given by equation [4]. With the inertia assumed for the generator, the torque at the expander shaft end is given by equation [5].

$$M_{se exp} = M_{ag} \left(\frac{J_{exp}}{J_{exp} + J_{gen}} \right) = M_{ag} J_{ratio} \left(\frac{1}{1 + J_{ratio}} \right) \quad (4)$$

$$M_{se exp} \cong 0.074 M_{ag} \quad (5)$$

where $J_{ratio} = J_{exp}/J_{gen}$

A conservative estimation for the electrical malfunctioning torque at the air gap can be obtained assuming a multiplication factor of 20 to the torque calculated with 153 MVA at 3000 rpm (314 rad/s). With this assumption, the peak torque to be withstood by the coupled end of the expander is 721 kNm

It can be seen that, in reason of the low J_{ratio} , the peak torque is only 1.74 times the normal torque (130 MW at 3000 rpm = 414 kNm), which is an advantage when designing the shaft end of the expander. DGS require an axial assembly and hence, if the shaft end of the expander is an integral piece of rotor, the diameter of the sleeves of the DGS needs to be greater than any other rotor diameter externally positioned with respect to the DGS. This assembly constraint, together with the fact that DGS are available only up to a certain size (approximately 350-400 mm), establishes a maximum dimension for the coupled shaft end which limits the maximum torque withstandable.

The inertia of the expander rotor is very small if compared to the generator rotor allowing an integral shaft end design with a tapered coupling (conicity 1/20) having a

maximum diameter of 320 mm. The coupling hub, dimensioned with an outer diameter of 480 mm (1.5 times the internal maximum diameter) and having an axial length of 384 mm (1.2 times the internal maximum diameter), when assembled with 0.25% interference is suitable for a slippage torque capacity (calculated with a friction factor of 0.15) of around 1100 kNm, sufficiently higher than the 721 kNm estimated as peak torque in case of electrical fault event. The DGS size finally selected has a diameter of 350 mm.

It is worth noting that the basic torsional sizing reported is impacted by the inertia of the expander rotor: a flow path designed at a larger diameter would have resulted in a larger J_{ratio} , resulting in the necessity to design a shaft end for a much larger torque. For example, with a $J_{ratio}=0.82$ (consistent with the larger flow path analysed: 4 stages on a 1280 mm hub diameter), the peak torque at the coupled shaft end would have been around 4400 kNm. Even assuming a very large coupled shaft end (suitable to withstand this torque) which is connected to the rest of the rotor by means of Hirth or spline connections, a DGS of 350 mm limits the journal bearing size to around 320 mm: a peak torque of 4400 kNm in the event of an electrical fault would result in 685 MPa of shear stress, which is an equivalent Von Mises stress of 1185 MPa. Such a huge equivalent stress would cause plastic deformation to the journal bearing collar (which, in general, is not desirable) with essentially any possible material selectable for the rotor.

The lateral analysis, section 5.2, has been executed with a coupling weight of 617 kg, consistent with a flexible coupling dimensioned for the peak torque capacity of 1100 kNm deriving by the presented torsional sizing.

6 CONCLUSION

This paper presented the aerodynamic-mechanical design integration of a 14-stage 130 MW turbine operating with a CO₂/SO₂ mixture. The design was initiated by defining the aerodynamic and mechanical constraints along with the required cycle boundary conditions, which were used to obtain the basic flow path through mean-line design. The mean-line flow path then formed the basis of the 3D blade design which was simulated and refined through 3D steady-state numerical simulation. Blade shape optimisation helped to further match the turbine boundary conditions with the required cycle constraints by maintaining the mass flow rate within 1% of the cycle mass flow rate for the given pressure ratio, while improving the performance by 2.7% from 90.2% to 92.9% and meeting safety and operational constraints.

Different exhaust cross sections, satisfying geometrical constraints, are investigated and the final selection is made to minimise the aerodynamic losses. The selected exhaust geometry steady state results showed a reduction of 0.34% in the turbine power developed from the whole turbine stages while the drop in the last stage power approaches 2.08%. The calculated alternating stresses on the last rotor stage are found acceptable compared to the high cycle fatigue properties of Nickel based alloys.

Unsteady CFD model of the last stage full annulus and the exhaust section is used to calculate the aerodynamic load fluctuations on the blade. The results showed a time average force magnitude 6.1% higher than the steady state results. The time domain is converted to frequency domain while a strong effect of the 4xREV frequency is captured compared to the

42xREV and 47xREV frequencies corresponding to the number of rotor and stator blades, respectively, however, the blades excitations are stronger.

Different mechanical design components are presented for the proposed turbine. The aerodynamic loads on the blades are mechanically assessed while the results have shown that the mechanical design is safe. The rotor-dynamic behaviour is found acceptable with a sufficient stability margin, considering destabilizing effects (Alford and seals effects).

The Dry Gas seals are among the most critical components for the mechanical design of sCO₂ expanders. The installation of these seals is challenged by: high pressure, high temperature, and high speed. These conditions lead to high thermal loads on the seals which significantly over complicates the design as the maximum allowable temperature of the seals is limited to 220°C.

In this regard, a dedicated thermal management system has been designed. A cooling flow (at 160°C) of around 0.5% of the expander flow ensures a proper cooling of the DGS regions. Moreover, the balancing drum cooling system (~2.2% cooling flow at 450°C) allows to employ traditional stainless steel for the HP and LP casing, avoiding the use of expensive Ni-based alloys for the heaviest components of the turbine.

ACKNOWLEDGEMENTS

This work was supported by the European Union's Horizon 2020 research and innovation programme under grant agreement No. 814985.

REFERENCES

- [1] White, M. T., Bianchi, G., Chai, L., Tassou, S. A., and Sayma, A. I., 2021, "Review of supercritical CO₂ technologies and systems for power generation," *Applied Thermal Engineering*, 185, p. 116447. 10.1016/j.applthermaleng.2020.116447
- [2] Yin, J. M., Zheng, Q. Y., Peng, Z. R., and Zhang, X. R., 2020, "Review of supercritical CO₂ power cycles integrated with CSP," *International Journal of Energy Research*, 44(3), pp. 1337-1369. 10.1002/er.4909
- [3] Binotti, M., Marcoberardino, G. D., Iora, P., Invernizzi, C., and Manzolini, G., "Scarabeus: Supercritical carbon dioxide/alternative fluid blends for efficiency upgrade of solar power plants," *Proc. AIP Conference Proceedings*, AIP Publishing LLC, p. 130002. 10.1063/5.0028799
- [4] Meng, F., Wang, E., Zhang, B., Zhang, F., and Zhao, C., 2019, "Thermo-economic analysis of transcritical CO₂ power cycle and comparison with Kalina cycle and ORC for a low-temperature heat source," *Energy Conversion Management*, 195, pp. 1295-1308. 10.1016/j.enconman.2019.05.091
- [5] Binotti, M., and Manzolini, G., "Supercritical carbon dioxide/alternative fluids blends for efficiency upgrade of solar power plant," *Proc. 3rd European supercritical CO₂ conference*, September 19-20, 2019, Paris, France, DEU, pp. 141-149. hdl.handle.net/11311/1154065
- [6] Morosini, E., Ayub, A., di Marcoberardino, G., Invernizzi, C. M., Iora, P., and Manzolini, G., 2022, "Adoption of the CO₂+ SO₂ mixture as working fluid for transcritical cycles: A thermodynamic assessment with optimized equation of state," *Energy Conversion Management*, 255, p. 115263. 10.1016/j.enconman.2022.115263
- [7] Crespi, F., de Arriba, P. R., Sánchez, D., and Muñoz, A., 2022, "Preliminary investigation on the adoption of CO₂-SO₂ working mixtures in a transcritical Recompression cycle," *Applied Thermal Engineering*, 211, p. 118384. 10.1016/j.applthermaleng.2022.118384
- [8] Zhang, H., Zhao, H., Deng, Q., and Feng, Z., "Aerothermodynamic design and numerical investigation of

- supercritical carbon dioxide turbine," *Proc. Turbo Expo: Power for Land, Sea, and Air*, American Society of Mechanical Engineers, p. V009T036A007. 10.1115/GT2015-42619
- [9] Shi, D., Zhang, L., Xie, Y., and Zhang, D., 2019, "Aerodynamic design and off-design performance analysis of a multi-stage S-CO₂ axial turbine based on solar power generation system," *Applied Sciences*, 9(4), p. 714. 10.3390/app9040714
- [10] Bidkar, R. A., Mann, A., Singh, R., Sevincer, E., Cich, S., Day, M., Kulhanek, C. D., Thatte, A. M., Peter, A. M., Hofer, D., and Moore, J., 2016, "The 5th International Symposium-Supercritical CO₂ Power Cycles Conceptual Designs of 50MW e and 450MW e Supercritical CO₂ Turbomachinery Trains for Power Generation from Coal. Part 1: Cycle and Turbine." [11] Kim, W. J., and Song, S. J., "Rotordynamic Forces Due to Rotor Sealing Gap in Axial Turbines," *Proc. Turbo Expo: Power for Land, Sea, and Air*, pp. 305-315. 10.1115/GT2003-38616
- [12] Uysal, S. C., White, C. W., Weiland, N., and Liese, E. A., 2022, "Cooling analysis of an axial turbine for a direct fired sCO₂ cycle and impacts of turbine cooling on cycle performance," *Energy Conversion and Management*, 263, p. 115701. 10.1016/j.enconman.2022.115701
- [13] Ehrich, F. F., 1999, "Handbook of Rotordynamics, revised edition, Chapter No. 1.6," Krieger Publishing Company, Malabar, Florida.
- [14] Salah, S. I., Khader, M. A., White, M. T., and Sayma, A. I., 2020, "Mean-line design of a supercritical CO₂ micro axial turbine," *Applied Sciences*, 10(15), p. 5069. 10.3390/app10155069
- [15] Fu, J., Liu, J., and Zhou, S., 2007, "Experimental and numerical investigation of interaction between turbine stage and exhaust hood," *Journal of Power Energy*, 221(7), pp. 991-999. 10.1243/09576509JPE415
- [16] George, T. J., Shen, M.-H. H., Scott-Emuakpor, O., Nicholas, T., Cross, C. J., and Calcaterra, J., 2005, "Goodman diagram via vibration-based fatigue testing," *Journal of Engineering Materials and Technology*, 127(1), pp. 58-64. 10.1115/1.1836791
- [17] Kalra, C., Hofer, D., Sevincer, E., Moore, J., and Brun, K., "Development of high efficiency hot gas turbo-expander for optimized CSP supercritical CO₂ power block operation," *Proc. The Fourth International Symposium—Supercritical CO₂ Power Cycles (sCO₂)*, Citeseer, pp. 1-11.
- [18] Wilkes, J., Robinson, K., Wygant, K., Pelton, R., and Bygrave, J., "Design and Testing of a 275 Bar 700 Degree Celsius Expander for an Integrally Geared Supercritical CO₂ Comander," *Proc. Turbo Expo: Power for Land, Sea, and Air*, American Society of Mechanical Engineers, p. V009T028A025. 10.1115/GT2022-83284
- [19] Guédez, R., Barberis, S., Maccarini, S., López-Román, A., Milani, A., Pesatori, E., Oyarzábal, U., and Sánchez, A., "Design of a 2 MW Molten Salt Driven Supercritical CO₂ Cycle and Turbomachinery for the SOLARSCO2OL Demonstration Project," *Proc. Turbo Expo: Power for Land, Sea, and Air*, American Society of Mechanical Engineers, p. V009T028A008. 10.1115/GT2022-82013
- [20] Stein, P., Pfoster, C., Sell, M., Galpin, P., and Hansen, T., "CFD modeling of low pressure steam turbine radial diffuser flow by using a novel multiple mixing plane based coupling: Simulation and validation," *Proc. Turbo Expo: Power for Land, Sea, and Air*, American Society of Mechanical Engineers, p. V008T026A020. 10.1115/GT2015-42632
- [21] Živný, A., Macálka, A., Hoznedl, M., Sedlák, K., Hajsman, M., and Kolovratník, M., "Numerical Investigation and Validation of the 1090 MW Steam Turbine Exhaust Hood Flow Field," *Proc. Turbo Expo: Power for Land, Sea, and Air*, American Society of Mechanical Engineers, p. V008T029A015. 10.1115/GT2017-63576
- [22] Fu, J.-L., Liu, J.-J., and Zhou, S.-J., 2012, "Unsteady interactions between axial turbine and nonaxisymmetric exhaust hood under different operational conditions," *Journal of Turbomachinery*, 134(4): 041002 (11 pages). 10.1115/1.4003647
- [23] Salma Salah, Francesco Crespi, Martin White, Antonio Munoz, Andrea Paggini, Marco Ruggiero, David Sanchez, and Sayma, A., 2023, "Axial turbine flow path design for concentrated solar power plants operating with CO₂ blends (Submitted for publication)," *Applied thermal engineering*.
- [24] Kim, H. S., Cho, M., and Song, S. J., 2003, "Stability analysis of a turbine rotor system with Alford forces," *Journal of Sound Vibration*, 260(1), pp. 167-182. 10.1016/S0022-460X(02)00926-4
- [25] Oleksak, R. P., and Rouillard, F., 2020, "4.14 - Materials Performance in CO₂ and Supercritical CO₂," *Comprehensive Nuclear Materials (Second Edition)*, R. J. M. Konings, and R. E. Stoller, eds., Elsevier, Oxford, pp. 422-451.
- [26] 2020, E. H., 2021, "DESOLINATION: DEMonstration of concentrated SOLAR power coupled with advaNced desAlinaTion system in the gulf regION."
- [27] Liao, X., Chalumeau, S., Crespi, F., Prieto, C., Lopez-Roman, A., Rodriguez de Arriba, P., Martinez, N., Sánchez, D., Paggini, A., and David, P., "Life Cycle Assessment of Innovative Concentrated Solar Power Plants Using Supercritical Carbon Dioxide Mixtures," *Proc. Turbo Expo: Power for Land, Sea, and Air*, American Society of Mechanical Engineers, p. V009T028A033. 10.1115/GT2022-83576
- [28] Bidkar, R. A., Sevincer, E., Wang, J., Thatte, A. M., Mann, A., Peter, M., Musgrove, G., Allison, T., and Moore, J., 2017, "Low-leakage shaft-end seals for utility-scale supercritical CO₂ turboexpanders," *Journal of Engineering for Gas Turbines and Power*, 139(2). 10.1115/1.4034258
- [29] Rafanelli, I., Generini, G., Andreini, A., Diurno, T., Girezzi, G., and Paggini, A., "Development and Validation of a Segregated Conjugate Heat Transfer Procedure on a sCO₂ Dry Gas Seal Test Bench," *Proc. Proceedings of Turbo Expo: Power for Land, Sea, and Air*, American Society of Mechanical Engineers. GT2023-101987.
- [30] Steinmann, D., Kassimi, R., Kleiner, J., Susini, P., Milani, A., and Dozzini, M., 2022, "Dry gas seals design for centrifugal compressors in supercritical CO₂ application," *7th International sCO₂ Power Cycles Symposium* San Antonio, Texas.
- [31] Abdeldayem, A., White, M. T., and Sayma, A. I., "Comparison of CFD predictions of supercritical carbon dioxide axial flow turbines using a number of turbulence models," *Proc. Turbo Expo: Power for Land, Sea, and Air*, American Society of Mechanical Engineers, p. V010T030A010. 10.1115/GT2021-58883
- [32] Jang, H. J., Kang, S. Y., Lee, J. J., Kim, T. S., and Park, S. J., 2015, "Performance analysis of a multi-stage ultra-supercritical steam turbine using computational fluid dynamics," *Applied Thermal Engineering*, 87, pp. 352-361. 10.1016/j.applthermaleng.2015.05.007
- [33] Aqel, O., White, M., and Sayma, A., "Binary interaction uncertainty in the optimisation of a transcritical cycle: consequences on cycle and turbine design," *Proc. 4th European sCO₂ Conference for Energy Systems: March 23-24, 2021*, Online Conference, pp. 164-176. 10.17185/dupublico/73942
- [34] Dubiez-Le Goff, S., Couturier, R., Guétaz, L., and Burlet, H., 2004, "Effect of the microstructure on the creep behavior of PM Udimet 720 superalloy—experiments and modeling," *Materials Science and Engineering: A*, 387, pp. 599-603.
- [35] Abdeldayem, A., White, M., Paggini, A., Ruggiero, M., and Sayma, A. I., 2022, "Integrated Aerodynamic and Structural Blade Shape Optimisation of Axial Turbines Operating with Supercritical Carbon Dioxide Blended with Dopants," *Journal of Engineering for Gas Turbines Power*, p. 144(110): 101016 (101012 pages). 10.1115/1.4055232
- [36] Salah, S. I., White, M. T., and Sayma, A. I., 2022, "A comparison of axial turbine loss models for air, sCO₂ and ORC turbines across a range of scales," *International Journal of Thermofluids*, p. 100156. 10.1016/j.ijft.2022.100156
- [37] Vance, J. M., Zeidan, F. Y., and Murphy, B. G., 2010, *Machinery vibration and rotordynamics*, Chapter No. 6, John Wiley & Sons.